X-ray spectroscopic studies of the electronic structure of chromium-based *p*-type transparent conducting oxides

E. Norton,[1,2,*] L. Farrell,[1,2] S. D. Callaghan,[1] C. McGuinness,[1] I. V. Shvets,[1,2] and K. Fleischer[1,2]
[1]*School of Physics, Trinity College, University of Dublin, Dublin 2, Ireland*
[2]*Centre for Research on Adaptive Nanostructures and Nanodevices (CRANN)*
(Received 8 January 2016; revised manuscript received 17 February 2016; published 7 March 2016)

The valence band structure of *p*-type transparent oxides—crystalline $Mg_xCr_{2-x}O_3$ and nanocrystalline Cu_xCrO_y—is analyzed as a function of incoming photon energy. The valence band of both *p*-type transparent conducting oxides shows striking similarities to measurements on crystalline $CuCrO_2$:Mg with all films showing that chromium states compose the top of the valence band, suggesting that the valence-band structure is dominated by the presence of the Cr-O_6 octahedra. A comparison of the valence band between the best performing *p*-type, crystalline $CuCrO_2$:Mg, with crystalline $Mg_xCr_{2-x}O_3$ and nanocrystalline Cu_xCrO_y shows that the chromium 3*d* states are fixed irrespective of changes in long-range crystallographic order. This indicates little spatial overlap between adjacent Cr 3*d* states. This further confirms the conduction mechanism via hopping for chromium based *p*-type TCOs as the Cr 3*d* states are localized within the Cr-O_6 octahedra.

DOI: 10.1103/PhysRevB.93.115302

I. INTRODUCTION

Optically transparent conductive materials (TCMs) such as conductive polymers, 2D materials like graphene, nanowires, and metal oxides offer the promise of fully transparent electronic devices [1,2]. Transparent conducting metal oxides (TCOs) are the most widely used TCMs by industry due to the excellent properties of *n*-type TCOs-indium tin oxide (ITO), fluorine-doped oxide (FTO), and aluminium-doped zinc oxide (AZO) [3]. However, fully transparent devices have been hindered by *p*-type TCOs having poor performance in terms of carrier mobility and transparency [4–7]. Moreover, very few materials show promise of stable bipolar doping [6,8], which if successful would open up the possibility of optically transparent CMOS technology [9].

In *p*-type TCOs, the main challenge has been to overcome that the valence-band maximum is composed largely of states with oxygen 2*p* character, which will hinder high mobility holes, converse to the *s*-like state conduction band minimum of metal oxides. The selection of an open *d*-shell transition metal has been crucial to obtain good performing *p*-type conductivity in TCOs [10]. Since the initial report by Kawazoe *et al.* [11], delafossites have attracted much attention as *p*-type TCO materials. The delafossite structure, ABO_2, has an *A* cation site linearly coordinated to the oxygen octahedra within which the B site cation resides. In particular, cuprous delafossites exhibit exceptional electrical, magnetic, and optical properties [12].

However, *p*-type films suffer from low mobilities and can typically only be estimated by the Seebeck effect. There are some exceptions such as $CuCrO_2$:Mg, which was measured by the AC Hall effect [13]. This limits their use in applications such as transparent transistors where mobility is paramount. Beyond the low mobility, *p*-type TCOs have relevance in photovoltaics as selective contacts for the extraction of holes to improve the overall efficiency and performance of solar cells [14–17]. Furthermore, a recent paper by Chen *et al.* shows *p*-type TCOs to be useful as a selective contact as well as a protective overlayer with *n*-type silicon for stable, efficient solar water splitting [18].

An appropriate figure of merit (FOM) to characterize the performance of a TCO is a ratio of electrical conductivity weighted against the optical absorption coefficient [19]. $CuCrO_2$:Mg exhibits the highest FOM to date [20]. The success of the cuprous delafossites in exhibiting exceptional electrical properties was attributed to copper 3*d* states reducing the oxygen 2*p* character at the top of the valence band through hybridization. Initially, the choice of chromium as the optimum *B* site cation was attributed to closed lattice matching of the two cation sites, which affected the optical properties fortuitously. Interestingly, a recent paper by Farrell *et al.* reports a copper deficient nanocrystalline $CuCrO_2$ [22] material with an FOM of 350 μS and conductivity as high as 12 S cm^{-1}. The Cu_xCrO_y films have an FOM an order of magnitude greater than $CuCrO_2$:Mg deposited previously by spray pyrolysis and also only an order of magnitude below the best FOM reported for $CuCrO_2$:Mg [23].

Theoretical studies of the electronic structure of *p*-type $CuCrO_2$ led to conflicting reports on the nature of the top of the valence band: whether it is predominately composed of Cu or Cr 3*d* states. The first reports from theoretical and experimental studies suggested that Cu states lay at the top of the valence band [24–26]. Further DFT+*U* studies by Scanlon and Watson, and experimental confirmation by Yokobori *et al.* using resonant valence-band photoemission spectroscopy (RVBPES) showed evidence that in fact chromium states predominately compose the top of the valence band [27,28].

Furthermore, a large range of chromium based *p*-type TCOs have been reported in the last 5 years: two corundum lattice structures—$Mg_xCr_{2-x}O_3$ [21,29] and $Ni_xCr_{2-x}O_3$ [30]—have been shown to be *p*-type TCOs. Several other reports of high figure of merit (FOM) *p*-type TCOs also contain chromium in an octahedral coordination. Besides the prototypical $Mg_xCr_{2-x}O_3$ and $Ni_xCr_{2-x}O_3$, these include $LaCrO_3$:Sr [31] and spinel structures such as Cr_2MnO_4:Li [32,33].

In this study, RVBPES has been carried out on films of $Mg_xCr_{2-x}O_3$ and Cu_xCrO_y with varying Cu/Cr ratio,

*nortonem@tcd.ie

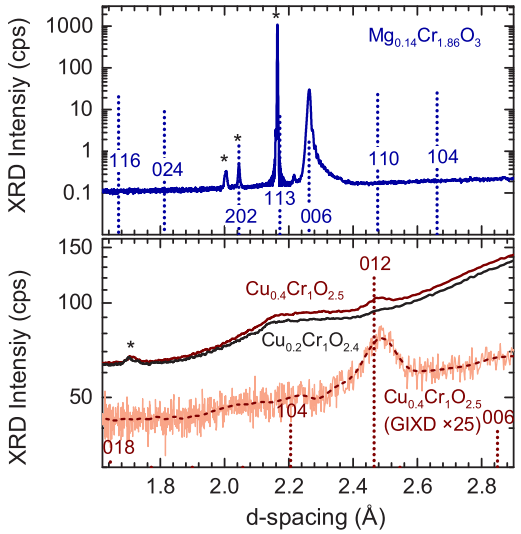

FIG. 1. X-ray diffraction of the analyzed samples. The top panel shows the epitaxially grown $Mg_xCr_{2-x}O_3$. Only the 006 reflex of the eskolaite phase is observed. The lower panel shows the data for the nanocrystalline Cu_xCrO_y. To illustrate the polycrystalline nature, a symmetric $\theta/2\theta$ measurement is compared to a grazing incidence measurement. Only the strongest $CuCrO_2$ reflex can be observed for the sample with higher copper content. Structures originating from the substrate and/or sample holders have been marked (∗).

providing qualitative experimental evidence about the composition of the valence band. Experimentally, we can probe this by using resonant photoemission spectroscopy (RPES). RPES is a technique that is often described as a two-step process: the creation of a core hole, and secondly the decay of that core hole. The decay of the core hole causes the emission of an Auger electron from the valence band. This valence electron has the same final state as an electron emitted by direct photoemission. However, these studies ideally have films that are sufficiently conductive to avoid shifts in binding energies due to sample charging, hence only highly conductive p-TCOs can be easily analyzed.

While several studies have been performed on crystalline $CuCrO_2$:Mg a comparison with $Mg_xCr_{2-x}O_3$ and Cu_xCrO_y will provide a general insight into the electronic structure and low mobility of chromium based p-type TCOs. Few studies of this nature have been carried out on conducting oxides. The Cu_xCrO_y films, an oxide synthesized at low temperatures, has been shown to be copper deficient with poor crystalline quality, yet possesses a high FOM. The defective material allows us, by altering the Cu/Cr ratio, to switch between two regions: a highly copper doped amorphous Cr_2O_3:Cu structure and a copper deficient $CuCrO_2$. While less conductive than the crystalline $CuCrO_2$:Mg, it has one of the highest FOMs, 350 μS, of any solution processed p-type TCOs [34].

The difference in the crystallographic properties is illustrated in the x-ray diffraction (XRD) patterns of the samples shown in Fig. 1. The $Mg_xCr_{2-x}O_3$ sample is epitaxially grown on c plane Al_2O_3 showing only the 006 reflex of the eskolaite phase. In contrast, the Cu_xCrO_y samples are nanocrystalline samples with a coherent domain size below 8 nm and no preferential growth direction. The phase identification in this case is difficult by XRD alone as the film signal is weak compared to the substrate and sample holder background. A more comprehensive study on the crystallographic properties by XRD and Raman spectroscopy has been published elsewhere [34]. Despite the poor crystallinity, the films are closed, smooth layers and can be readily incorporated in devices.

II. EXPERIMENTAL METHODS

Thin film samples of chromium oxide based p-type TCOs have been prepared by either molecular beam epitaxy (Cr_2O_3 based, crystalline films) or spray pyrolysis (copper deficient $CuCrO_2$). The $Mg_xCr_{2-x}O_3$ films were grown on $Al_2O_3(0001)$ substrates using a DCA M600 molecular beam epitaxy system (MBE) with base pressure of 1.3×10^{-7} Pa. E-beam evaporation was done from Cr_2O_3 pellets (99.9% Kurt J. Lesker) at an oxygen partial pressure 6×10^{-3} Pa with the substrate temperature maintained at 873 K. The doping was achieved by controlling the supplied power to a second e-beam evaporator loaded with MgO (99.95% Kurt J. Lesker) [21]. After growth, the $Mg_xCr_{2-x}O_3$ film was postannealed in oxygen for 2 h at a temperature of 973 K, showing an FOM of 3.5 μS ($\sigma \approx 0.04$ S cm^{-1}), a factor of three improvement on the as-grown film [21,35]. The $Mg_xCr_{2-x}O_3$ film showed a composition of $Mg_{0.12}Cr_{1.86}O_3$ when characterized by XPS, using a laboratory-based Omicron multiprobe system with monochromatic Al K_α x rays ($h\nu = 1486.7$ eV) and an EA125 analyzer.

Nanocrystalline, highly conductive, copper-deficient copper chromium oxide was grown by spray pyrolysis using a simple air blast nozzle. Copper(II) acetylacetonate and chromium(III) acetylacetonate precursors in a methanol solution were sprayed at 623 K on glass microscope slides [34]. The incorporated copper content of the Cu_xCrO_y films was controlled by altering the concentration of copper acetylacetonate in the initial precursor solution. The samples examined in this study are a high FOM (150 μS, $\sigma \approx 5$ S cm^{-1}) nanocrystalline film with a copper deficient composition, $Cu_{0.40}Cr_1O_{2.5}$, and a lower FOM (4 μS, $\sigma \approx 0.15$ S cm^{-1}) film, which corresponds to a lower copper content, $Cu_{0.2}Cr_1O_{2.4}$. X-ray absorption spectroscopy (XAS), additional core level x-ray photoemission spectroscopy (XPS), and resonant valence-band photoemission spectroscopy (RPES) were carried out at the D1011 beamline at MAX II, MAX-lab, Sweden. All photoemission spectra were normalized by the ring current and the beam line transfer function measured by a reference total electron yield on a clean gold mesh. The valence-band spectra at photon energies of 40–100 eV were taken with a fixed exit slit and a photon flux of between 10^{11}–10^{12} ph/s incident on the sample. The binding energies in valence-band spectra were aligned to the Fermi edge taken of tantalum foil in contact with the sample. All XAS absorption spectra were taken in total electron yield (TEY) mode by measuring the drain current as a function of incident photon energy. XRD patterns have been measured with a Bruker D8 Discover using a monochromated Cu-K_α source (epitaxial film and grazing incidence measurement) as well as a Bruker D8 Advance using a Mo-K_α source (Powder XRD for nanocrystalline films). Cr_2O_3 atomic multiplet calculations were carried out with the CTM4XAS software [36].

III. RESULTS

A. Surface preparation

The deposition methods required to prepare $Mg_xCr_{2-x}O_3$ and $CuCrO_2$ films limit studies to *ex situ* characterization. As-grown films are contaminated by surface carbon obscuring the measurement of the valence-band spectra. Hence all films were Ar sputtered with a beam energy of 1 keV at 4×10^{-4} Pa at grazing incidence to remove carbon and residuals of unreacted precursors from the surface prior to measurements. This was repeated in 4-minute steps at a time until a surface sensitive XPS scan of the C 1*s* core level taken at an incident photon energy of 380 eV would reveal minimal or no surface carbon present.

However, particularly in the case of $CuCrO_2$, valence band changes have been reported in crystalline thin films due to surface preparation [12]. As our Cu_xCrO_y thin films on glass are polycrystalline in nature, they will not have a coherent surface termination unlike *in situ* cleaved single crystals. Therefore introducing further disorder is unlikely to produce spectral differences in the valence band unlike in the case of Shin *et al.* studying crystalline $CuCrO_2$. Nevertheless, the effects of argon sputtering and annealing on the core levels and absorption spectra is discussed to quantify any differences.

X-ray photoelectron spectroscopy (XPS), Fig. 2, shows little change in the core level of the copper $2p_{3/2}$ peak in the Cu_xCrO_y thin films due to sputtering and annealing. The only observable difference is an increase in the asymmetry of the copper peak after oxygen annealing with greater weight at the low binding energy side.

This observation correlates with significant changes in the copper $L_{2,3}$ edge, (Fig. 2) with oxygen annealing. The prepeak at $h\nu \approx 926$ eV, which has been reported as an XAS final state of $2p3d^{10}$, which corresponds to an initial $3d^9$ state, i.e., Cu^{2+} impurities, is observed in the as-grown films and re-emerges with oxygen annealing [37]. The same prepeak, but significantly reduced in argon sputtered samples, is observed for Mg doped $CuCrO_2$ and stoichiometric $CuCrO_2$ [26,28]. In our Cu_xCrO_y films, it decreases with, but is not eliminated by argon sputtering and re-appears with oxygen annealing. The residual peak after sputtering is representative of the bulk film which has been characterised extensively in previous studies and seems consistent with $CuCrO_2$:Mg [21,34]. We suggest that due to the defective nature of our films the surface sites are preferentially oxidised, changing the copper oxidisation state locally on the surface but not in the bulk.

B. X-ray absorption spectroscopy

X-ray absorption spectroscopy (XAS) was performed on all films, after surface preparation. Soft x rays in the photon energy range of 40–1500 eV allowed us to probe the Cr *L*-edge absorption in Cu_xCrO_y and $Mg_xCr_{2-x}O_3$ films as well as the Cu *L* edge in Cu_xCrO_y films (see Fig. 3).

All absorption spectra have been normalised to the maximum intensity after background subtraction to compare features. A reference spectra of an epitaxial Cr_2O_3 film was taken; comparison with our $Mg_xCr_{2-x}O_3$ and Cu_xCrO_y films shows the chromium oxidation state unchanged. The Cr *L* edge for both $Mg_xCr_{2-x}O_3$ and Cr_2O_3 show an overall sharper structure than in the Cu_xCrO_y films. The epitaxial nature of the $Mg_xCr_{2-x}O_3$ creates a more ordered local coordination of the chromium atoms than the nanocrystalline Cu_xCrO_y with random crystal axis orientation. Spectral features remain consistent across the films though.

A reduction in intensity of the Cu L edge is seen for different films, which correlates with a reduction in Cu content from $Cu_{0.2}Cr_1O_{2.4}$ compared to the higher FOM, $Cu_{0.4}Cr_1O_{2.5}$ film. Unlike the chromium absorption spectra, the assignment of a clear oxidation state and electronic structure with a cuprite phase, Cu_2O (Cu^{+1}), is difficult. The copper x-ray absorption spectra has been notoriously difficult to analyze. Nominally, this oxidation state will have fully occupied copper 3*d* states in the valence band and an empty Cu 4*s* conduction band. The

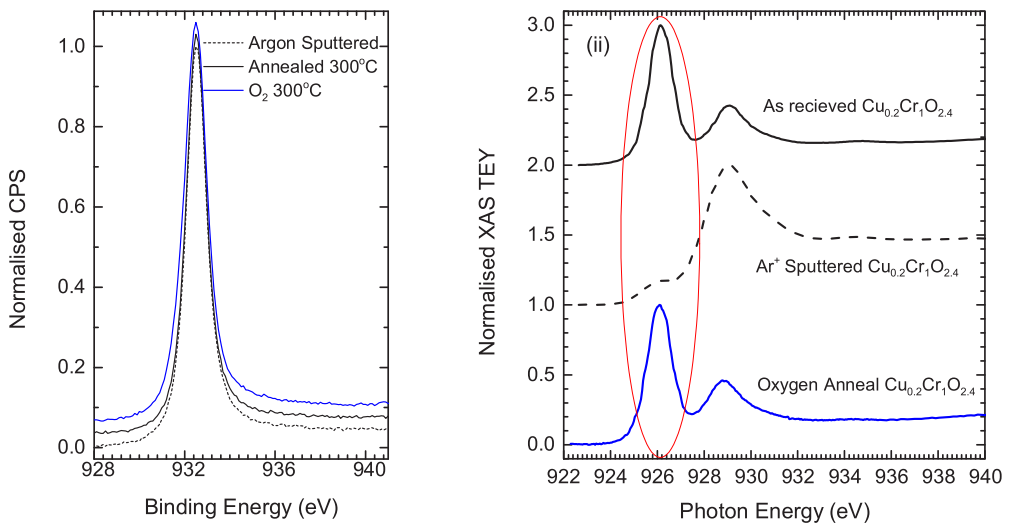

FIG. 2. (i) X-ray photoelectron spectroscopy of $CuCrO_2$ films highlighting the core level changes when the sample is argon sputtered and annealed in oxygen. A slight increase in the peak asymmetry is noted when the film is annealed in oxygen. (ii) In contrast, spectra of the Cu $L_{2,3}$ edge as a function of surface preparation. A large pre-peak, circled, is observed at $h\nu = 926$ eV in as received Cu_xCrO_y films. Argon sputtering reduces, but does not eliminate this peak entirely. Oxygen annealing after argon sputtering reproduces the same prepeak.

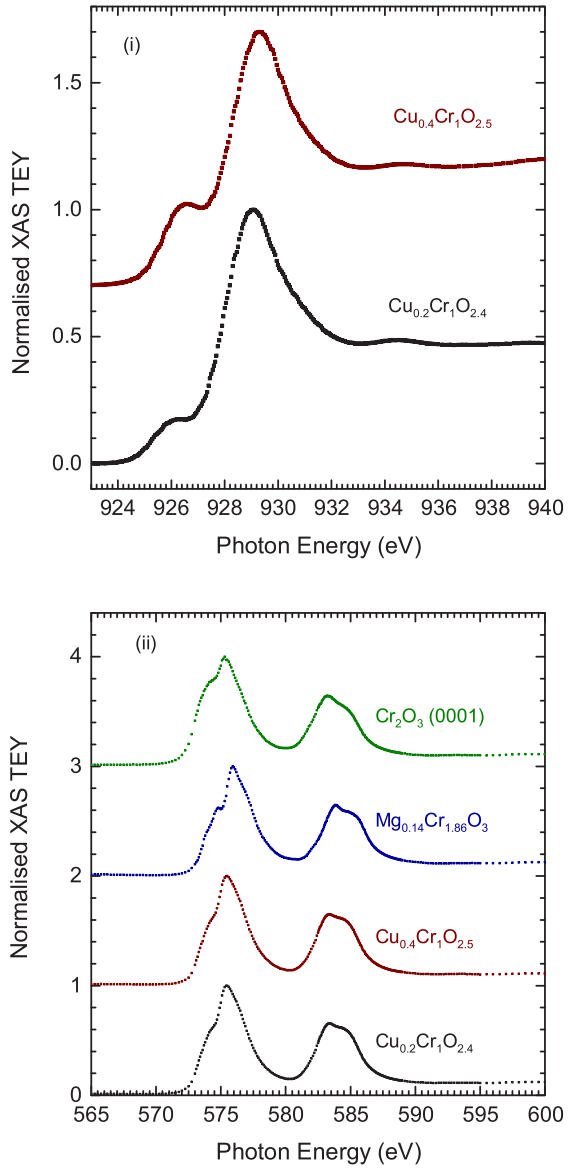

FIG. 3. (i) X-ray absorption spectra of the Cu $L_{2,3}$ of $Cu_{0.2}Cr_1O_{2.4}$ and $Cu_{0.4}Cr_1O_{2.5}$ and (ii) Cr $L_{2,3}$ edge of $Cu_{0.2}Cr_1O_{2.4}$, $Cu_{0.4}Cr_1O_{2.5}$, and $Mg_xCr_{2-x}O_3$.

band-structure calculations show Cu_2O to have substantial $3d$ character in the conduction band and conversely $4s$ character in the valence band [38]. However, experimentally the Cu L edge is difficult to analyze as x-ray spectroscopic investigations are nearly always overly sensitive to a mixed ground state as $2p$ edge core level spectroscopy is dominated by atomic multiplet effects as noted for instance in resonant inelastic x-ray spectra (RIXS) of Cu_2O being dominated by $3d \rightarrow 3d^*$ transitions [39].

In Fig. 3, the structure in the Cu L-edge around 926 eV is found to be more intense in the better conducting $Cu_{0.4}Cr_1O_{2.5}$ sample even after sputtering. A similar structure was found to appear in Mg doped $CuCrO_2$, increasing in intensity with magnesium concentration by Yokobori *et al.* [28]. The appearance of the same structure in copper deficient material suggests that the origin of the peak is a copper atom in a different electronic configuration in some defect complex involving the copper site and, e.g., an adjacent oxygen interstitial (O_i). In $CuCrO_2$, these defect complexes might be generated by magnesium substitution, while they natively occur in our defective Cu_xCrO_y.

DFT calculations of single point defects in $CuCrO_2$ have shown that V_{Cu} are the most readily formed intrinsic defects, while Mg_{Cu} is the dominant defect in doped materials [27]. However, no evaluation of complex defects such as Mg_{Cu}–V_{Cu} or V_{Cu}–O_i has been performed yet. In the related Cu_2O, it has already been shown that the formation of defect complexes readily occurs, explaining, e.g., why Sr^{+2} doping in Cu_2O leads to p-type conductivity as the p-type Sr_{Cu}–V_{Cu} defect complex is more likely to form than the n-type Sr_{Cu} isolated point defect [40]. In a similar fashion, other native defect complexes in $CuCrO_2$ could be contributing factors. The identification of their detailed nature would require *ab initio* analysis of many possible combinations including Cr_{Cu}–V_{Cu}, O_i–V_{Cu} and others. The observed structure for surfaces exposed to air or oxygen annealing would indicate an increase in the number of some defect like complexes. The fact that this increase is not observed by vacuum annealing alone and the Cr L edge is not affected leads to the identification of a Cu-O_i defect complex as a likely candidate not only for the changed surface termination but also as a contributing factor in the bulk doping of the material itself.

C. Resonant photoelectron spectroscopy

Figure 4 outlines the valence-band spectra of the $Mg_xCr_{2-x}O_3$ film over a range of photon energies. Two possible processes leading to the final state $3d^{n-1}$ are possible. The direct process of emitting a valence electron is possible for all incident photon energies greater than the valence electron binding energy,

PES: $3d^n + h\nu \rightarrow 3d^{n-1} + e^{-1}$.

However, if we have a tunable photon energy, we can generate a second process, outlined below for a $3p \rightarrow 3d$ transition:

RPES: $3d^n + h\nu \rightarrow 3p^5 \frown 3d^{n+1} \rightarrow 3p^6 3d^{n-1} + e^{-1}$.

While directly photoemitted electrons (PES) provide non-selective sampling of the atomic electronic levels, resonant photoemission spectroscopy (RPES) can be used to probe them selectively. By taking the same valence-band spectra collected at different photon energies, any increase in the intensity of a specific feature would indicate an increase, in our case, of $3d^{n-1}$ electrons emitted by photoemission through the intermediate resonant process.

Figure 4(ii) plots the valence-band photoemission intensity at a given binding energy as a function of the photon energy over the $3p$-$3d$ threshold and upwards. At the top of the valence band, two resonance features of interest are seen: a weak spectral response at 44–46 eV (red box) at a binding energy of 2.7 eV and a stronger resonant behavior at 48–50 eV (black box) at a slightly higher binding energy of 3 eV. The expected $3p$-$3d$ spectrum can be modeled using CTM4XAS software so we can see if the origin of this double peak feature can be pinpointed [36]. For the atomic multiplet calculation the value of the crystal-field parameter, 10 D_q, was chosen to be 2.03 eV; a value derived from the optical $2T_g$-$2A_g$ transition observed

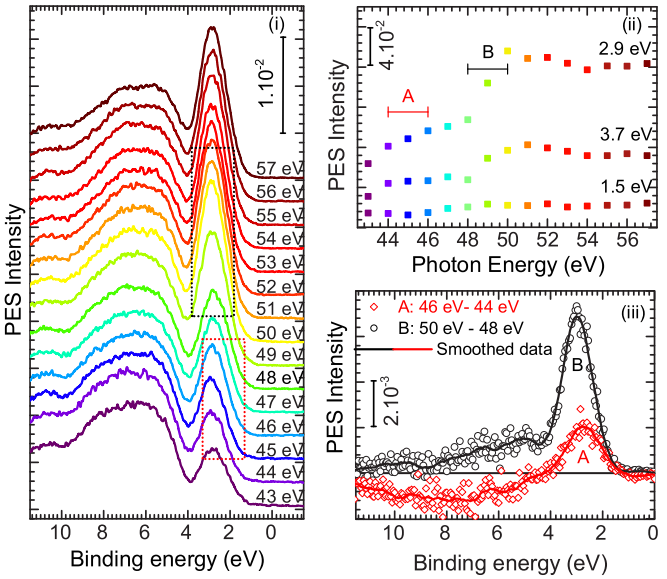

FIG. 4. (i) Valence-band spectra of the $Mg_{0.12}Cr_{1.86}O_3$ film over the photon energies 43 to 57 eV with an FOM of 3.5 μS. The black box in (i) indicates the region where resonant behavior over 48–50 eV is observed. The red box indicates the lower resonance over 44–46 eV. (i) PES intensity for selected binding energies as a function of incident photon energy. The strong enhancement around 49 eV is caused by a resonance to Cr $3p$–$3d$ transitions. A weaker enhancement is seen around 45 eV. (iii) Differences between the spectra at 50 and 48 eV (○) reveal the strong Cr resonance around 3 eV and an increase of PES intensity of 0.007. The spectral difference between 46 and 44 eV (◇) shows the onset of that resonance with reduced PES intensity (0.002). The negative differential signal in the 4–8 eV range is caused from going off-resonance to the oxygen p states.

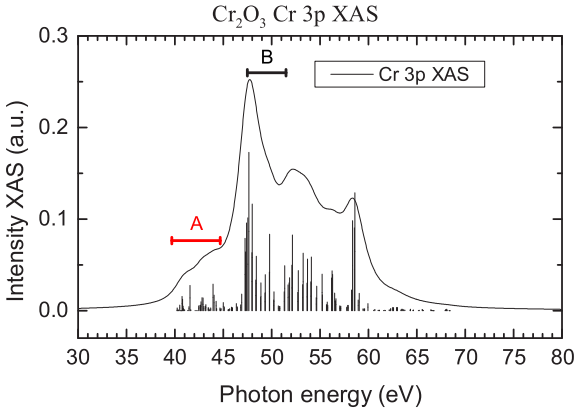

FIG. 5. Cr $M_{3,2}$ XAS spectrum with the distribution of intensities as obtained in a charge transfer atomic multiplet calculation. Feature A: 40–45 eV is due to a dominant transition to a low-spin XAS final state of $2p^5 3d^4$ (t_{2g}^4). The more intense feature B at higher excitation energies (49–55 eV) is the much more strongly allowed high-spin XAS final state of $2p^5 3d^4$ ($t_{2g}^3 e_g^1$).

in the pure epitaxially grown Cr_2O_3 films. This crystal-field splitting is broadly consistent with that observed from pure single crystals of Cr_2O_3 where it was found to be 2.08 eV [41]. Although a trigonal distortion away from O_h to C_3 symmetry is present in the corundrum lattice, the effect of such a distortion on the optical spectra is very small and various cluster and multiplet calculations effectively ignore this distortion as a result [42,43].

The Cr $2p$ and $3p$ XPS, $L_{3,2}$ and $M_{3,2}$ XAS are all best modelled taking into account charge transfer multiplets. A model for such charge transfer parameters has been previously put forward by Matsubara *et al.* [44] who successfully modeled Cr_2O_3 XAS, $2p$ XPS, and $2p$-$3d$ resonant inelastic x-ray scattering (RIXS) data. These same charge transfer energies are used in the present modeling. The $L_{3,2}$ XAS and $2p$ XPS are modeled with core hole lifetimes for the $L_3\,2p_{3/2}$ hole of 0.32 eV and the $L_2\,2p_{1/2}$ hole of 0.76 eV as recommended by Campbell and Papp [45], with an instrumental broadening of 0.1 eV and 0.3 eV, respectively. Our model reproduces the expected spectral features seen in the Cr $2p$ and $3p$ XPS, and $L_{3,2}$ XAS.

Figure 5 shows a plot of the $M_{3,2}$ absorption edge. This edge and $3p$ XPS are modeled with core hole lifetimes of 1.2 eV for the $M_{3,2/3p}$ holes and similar instrumental broadening. In Fig. 5, two features A and B are present in the $3p$ XAS spectra. Feature A, the lower excitation energies of 40–45 eV, is due to a dominant transition to a low spin XAS final state of $2p^5 3d^4$ (t_{2g}^4). The more intense feature, B, at higher excitation energies (49–55 eV) is the much more strongly allowed high spin XAS final state of $2p^5 3d^4$ ($t_{2g}^3 e_g^1$) as previously remarked by both Li *et al.* and Bertel *et al.* [46,47]. In the case of the $M_{3,2}$ edge, the atomic multiplet nature of the transitions dominate the intensity profile interlinked with the density and intensity of the allowed transitions to the given XAS final states. Although these are the XAS final states, they are the intermediate state in the $3p$-$3d$ VB RXPS spectrum and thus govern at what excitation energy the observed VB RXPS occurs at and also how intense that feature will be. The origin of the features A and B in Fig. 4 in the $Mg_xCr_{2-x}O_3$ film across the $3p$-$3d$ resonance can be linked to a difference in energy between the high- and low-spin states (t_{2g}^4) and ($t_{2g}^3 e_g^1$), which are the intermediate states for RPES.

Figure 6 shows similar measurements for the investigated Cu_xCrO_y films over the same Cr $3p$-$3d$ photon energy range. The strongest spectral feature at a binding energy of 2.6 eV, for the highest FOM Cu_xCrO_y sample, is resonant between the photon energy of 48–50 eV. The intensity of this Cr $3p$-$3d$ resonance is broader and less intense by a factor of nearly two compared to the $Mg_xCr_{2-x}O_3$ film. The onset of resonance is composed of one broad peak in contrast to the $Mg_xCr_{2-x}O_3$ films, which has two distinct onsets of resonance. The disordered nature of the films and lack of long-range order would lead to a breakdown of crystal-field symmetry rules for an energetic splitting of the t_{2g} and e_g levels, which leads to the absence of these features in all Cu_xCrO_y films. Other than that detail the differential spectra shows striking similarity to the one of the crystalline $Mg_xCr_{2-x}O_3$ film, suggesting the importance of the chromium octahedra in the electronic composition of the valence band of the higher FOM Cu_xCrO_y sample.

These observations show that a strong chromium composition must occupy the top of the valence band for these three p-type films. This correlates well with the previous works by Yokobori *et al.* on crystalline $CuCrO_2$:Mg films where the

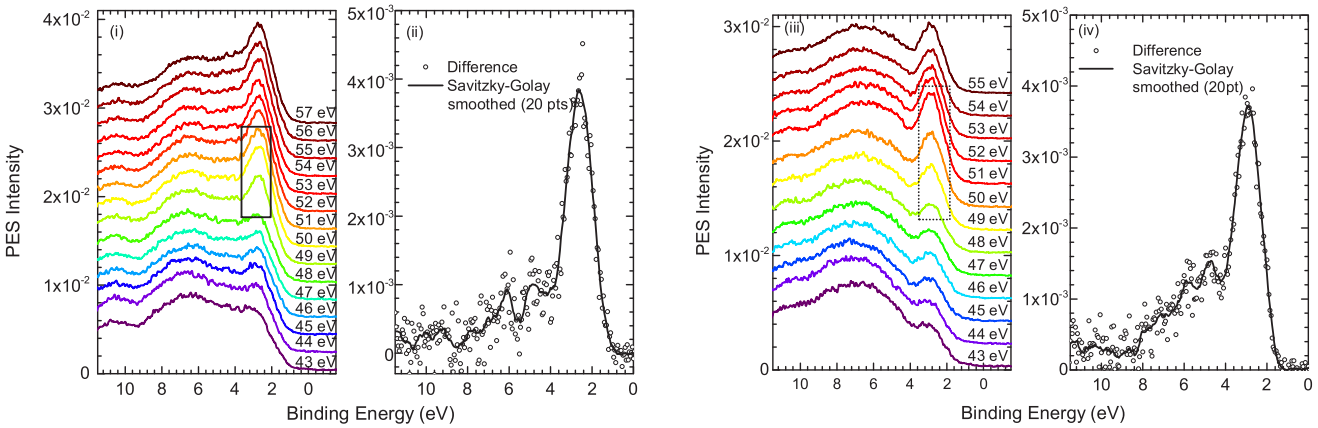

FIG. 6. The black box in (i) and (iii) indicates the region where resonant behavior is exhibited between 48 and 50 eV in (i) and 48 and 51 eV for (iii). Plots (ii) and (iv) show the difference spectra between 50–48 eV in (ii) and 51–48 eV in (iv). (ii) Peak fitting shows the sharp onset of resonance to be at a binding energy of 2.6 eV with a FWHM = 1.6 eV and an increase of PES intensity is 0.004 from 48–51 eV at 2.6 eV binding energy for the high FOM Cu_xCrO_y sample. (iv) The lower FOM sample shows the sharp onset of resonance to be at a binding energy of 3 eV with a FWHM of 1.7 eV, with a PES intensity increase equal to 0.004.

top of the valence band exhibits a strong chromium resonance around the Cr $3p$-$3d$ transition. For *in situ* cleaved samples, the increase in photoemission intensity at resonance was 0.003, in line with the observed intensity changes in the copper deficient Cu_xCrO_y films investigated here [28].

The Cu $3d$ states are also expected in the valence-band region of Cu_xCrO_y films. However, no copper resonance is seen, as outlined in Fig. 7. Stoichiometric, crystalline $CuCrO_2$:Mg shows a weak resonance around the Cu $3p$-$3d$ transition, approximately a factor of four smaller than for the Cr $3p$-$3d$ transition [28]. In contrast to these measurements, the Cu_xCrO_y films are substantially copper deficient and crystallographically disordered [34]. We also do not observe the two charge transfer satellites at 13 and 15 eV corresponding to Cu^+ ($3d^{10}$) and Cu^{2+} ($3d^9$) like initial states that Yokobori *et al.* observed. It would be expected that a broadening and reduced intensity, due to a lower copper content, could render the copper resonance and charge transfer satellites unresolvable in this case, while also being further complicated by the delocalized nature of copper d states due to the on-site $3d4s$ hybridization which introduces $4s$ character into the valence band. Within the signal to noise ratio, the lack of any observed copper resonance sets an upper limit on any resonant behavior. This upper limit of a weak copper resonance and a strong chromium resonance lends some support to the proposed mechanism by Yokobori *et al.* that the ground state of $CuCrO_2$ is showing signs of a Cu $4s$-Cr $3d$ charge transfer in $CuCrO_2$ films via O $2p$.

D. Valence-band composition

In order to assess the contribution of copper states qualitatively in the valence band of the Cu_xCrO_y films, we can compare the shape of the valence-band PES spectra taken off-resonance at an incident photon energy of 85 eV for samples with different copper content. The valence-band spectra are shown in Fig. 8, taken at an off-resonant photon energy of 85 eV for both nanocrystalline Cu_xCrO_y and crystalline $Mg_xCr_{2-x}O_3$ films. They have been compared with previous measurements on crystalline $CuCrO_2$:Mg [28]. For a meaningful comparison, all spectra were aligned to the same valence-band maximum position of $CuCrO_2$:Mg; which coincided with the Fermi level at 0 eV due to the high doping levels of the material. The absolute valence-band maximum

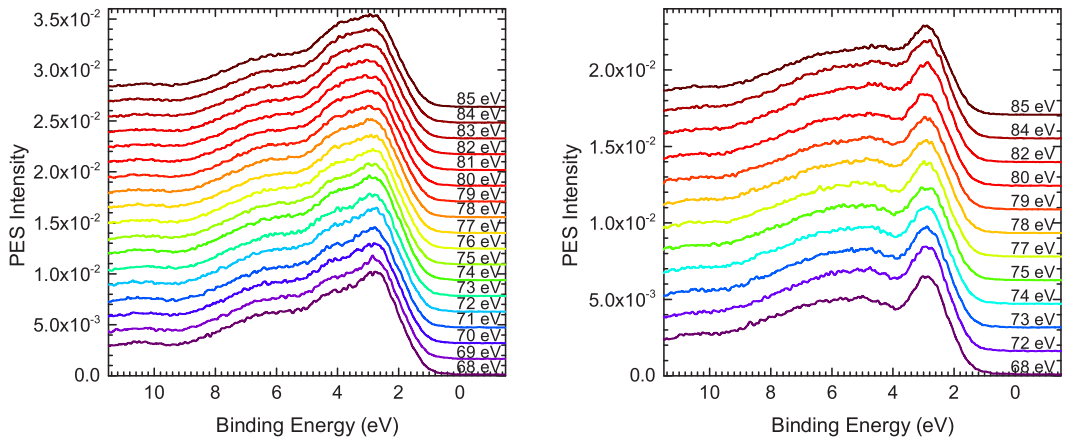

FIG. 7. Valence-band spectra of Cu_xCrO_y films over the photon energies 68–85 eV, probing the copper $3p$-$3d$ resonance.

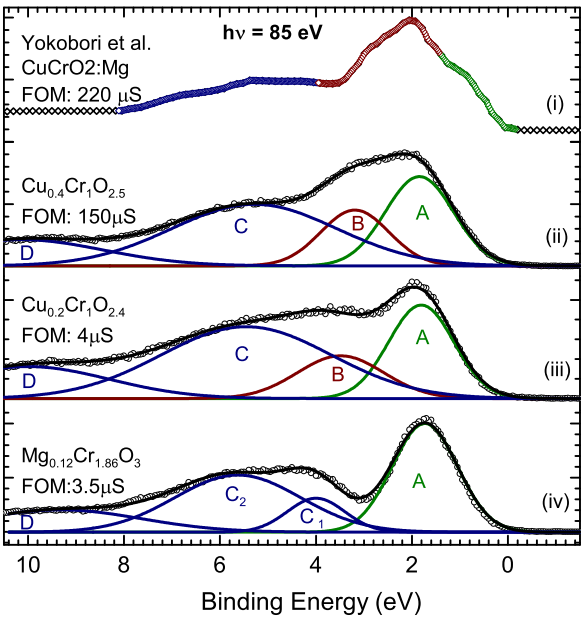

FIG. 8. Valence-band spectra of all *p*-type films compared at the photon energy of 85 eV. For comparison, all spectra have been aligned to the valence-band maximum of $CuCrO_2$:Mg [28] to account for shifts in the Fermi level of the different oxide films.

position for $Cu_{0.4}Cr_1O_{2.5}$, $Cu_{0.4}Cr_1O_{2.5}$, and $Mg_{0.12}Cr_{1.86}O_3$ lie 0.8, 1, and 1 eV below the Fermi level (seen in Figs. 4 and 6).

Density functional theory (DFT) can model the composition of the valence-band spectra. In fact, studies have been carried out previously for Cr_2O_3 [46], $CuCrO_2$ [26], and $CuCrO_2$:Mg [28]. No in-depth study has been carried out for *p*-type $Mg_xCr_{2-x}O_3$. However, as mentioned previously, some discrepancy can arise about the best parameters to model a particular material. Experimental reports become crucial to providing qualitative evidence for modeling material properties.

Our measurements have been fitted with Gaussian peaks, in order to deconvolute prominent features in the VBM PES data. Best fits were obtained for all spectra containing four components. The dominant structure (peak A) in these fits is attributed to the Cr 3*d* states, as the position and width coincides with the Cr 3*d* partial density of states extracted from the differential valence-band PES (Figs. 4 and 6). This matches previous reports for both $CuCrO_2$:Mg and Cr_2O_3 films [28,46].

The spectral features of Yokobori *et al.* [spectrum (i) in Fig. 8], were assigned by DFT calculations in their report with predominant oxygen *p* states lying between 4 and 8 eV (blue). We assume the O 2*p* states to lie in a similar energetic region for our Cu_xCrO_y films. While all Cu_xCrO_y films show a broad feature (labelled C) in this energy range, the crystalline Cr_2O_3 sample does show a fine structure (labelled C_1 and C_2) consistent with the valence-band structure of undoped Cr_2O_3 [48]. A similar fine structure in the Cr 3*d* states has not been resolved as a consequence of spectral broadening by the Mg incorporation.

As mentioned, across the copper 3*p*-3*d* threshold and upwards, no resonance was apparent in the studied Cu_xCrO_y films. However, comparing the spectra shape of the different valence bands, an additional structure is apparent for the Cu containing, polycrystalline films (Fig. 8, labeled B), when compared with the $Mg_xCr_{2-x}O_3$ films. Energetically, the structure is found 1–2 eV above the Cr 3*d* states and is found to be more intense in the sample of higher copper content. This lies in a similar region to the calculations for the Cu 3*d* states for crystalline $CuCrO_2$:Mg. If compared to the previously investigated crystalline material, all valence-band structures are significantly broadened, which is a consequence of the defective, nanocrystalline nature of the films. Equally, the ratio between the Cr 3*d* and Cu 3*d* intensity significantly differs from previous reports, as all films investigated here are copper deficient. In addition, the polycrystalline nature of thin films of glass will not have a coherent surface termination as *in situ* cleaved films, leading to the loss of fine structure in our measurements. It has been previously reported that the surface termination can significantly alter the valence-band shape in $CuCrO_2$ [12].

IV. CONCLUSION

Resonant photoelectron spectroscopy was performed on several high figure of merit *p*-type TCOs; $Mg_xCr_{2-x}O_3$ (3.5 μS) and Cu_xCrO_y (150 μS) thin films. The top of the valence band seems to be composed largely of Cr 3*d* states in all the films and is not altered significantly with increasing copper content for Cu_xCrO_y films. This provides experimental evidence for the position of elemental states in the valence band of oxides featuring octahedral coordinated Cr sites. The observations explain why many recently discovered *p*-type TCOs such as Cr_2O_3:Mg, $LaCrO_3$:Sr, Cr_2MnO_4:Li, and even highly defective Cu_xCrO_y are showing similar good performance for *p*-type TCOs. The similarity of the Cr 3*d* partial density of states for all the investigated films also highlights the limitation of creating dispersion in the valence band by cation doping, which leaves the Cr-O_6 octahedra unchanged.

Our findings highlight that for Cr-based *p*-type TCOs the valence-band structure is dominated by the presence of the Cr-O_6 octahedra, independent of their long-range crystallographic order. This suggests that the Cr 3*d* states are highly localized within the Cr-O_6 octahedra further confirming hopping mechanisms for carrier transport previously discussed for these materials [21,31,49]. To increase the hole mobility, it is likely that this Cr-O_6 octahedral coordination has to be altered, e.g., by anion doping or strain.

However, this particular valence-band composition allows for good performing, noncrystalline Cr-based *p*-TCOs, which can therefore be synthesized via low-temperature processes like spray pyrolysis. The example of nanocrystalline Cu_xCrO_y illustrates that poor crystallinity is not necessarily detrimental to the figure of merit and opens new possibilities for applications were high hole mobilities are of less importance.

ACKNOWLEDGMENTS

This work was supported by the Irish Research Council under Grant No. GOI/PG/2013/445 and Science Foundation Ireland under Grant No. 12/IA/1264. Funding from the Higher

Education Authority under the Programme for Research in Third-Level Institutions scheme, Cycle 5 is also gratefully acknowledged. The research leading to these results has received funding from the European Community's Seventh Framework Programme (FP7/2007-2013) under Grant agreement No. 312284. We express our thanks to the MAX laboratory beamline staff in particular, A. Preobrajenski, K. Handrup and A. Generalov, for their help and technical assistance.

[1] G.-H. Lee, Y.-J. Yu, X. Cui, N. Petrone, C.-H. Lee, M. S. Choi, D.-Y. Lee, C. Lee, W. J. Yoo, K. Watanabe *et al.*, ACS Nano **7**, 7931 (2013).
[2] S. De, T. M. Higgins, P. E. Lyons, E. M. Doherty, P. N. Nirmalraj, W. J. Blau, J. J. Boland, and J. N. Coleman, ACS Nano **3**, 1767 (2009).
[3] H. Hosono, Thin Solid Films **515**, 6000 (2007).
[4] A. Banerjee and K. Chattopadhyay, Prog. Cryst. Growth Charact. Mater. **50**, 52 (2005).
[5] S. Sheng, G. Fang, C. Li, S. Xu, and X. Zhao, Physica Status Solidi (a) **203**, 1891 (2006).
[6] J. Robertson, R. Gillen, and S. Clark, Thin Solid Films **520**, 3714 (2012).
[7] G. Hautier, A. Miglio, G. Ceder, G.-M. Rignanese, and X. Gonze, Nat. Commun. **4**, 2292 (2013).
[8] H. Yanagi, H. Tomomi, S. Ibuki, K. Ueda, and H. Hosono, Appl. Phys. Lett. **78**, 1583 (2001).
[9] G. Thomas, Nature (London) **389**, 907 (1997).
[10] S. Lany, J. Phys.: Condens. Matter **27**, 283203 (2015).
[11] H. Kawazoe, M. Yasukawa, H. Hyodo, M. Kurita, H. Yanagi, and H. Hosono, Nature (London) **389**, 939 (1997).
[12] D. Shin, J. S. Foord, R. G. Egdell, and A. Walsh, J. Appl. Phys. **112**, 113718 (2012).
[13] M. O'Sullivan, P. Stamenov, J. Alaria, M. Venkatesan, and J. M. D. Coey, J. Phys.: Conf. Ser. **200**, 052021 (2010).
[14] X. Xu, J. Bullock, L. T. Schelhas, E. Z. Stutz, J. J. Fonseca, M. Hettick, V. L. Pool, K. F. Tai, M. F. Toney, X. Fang *et al.*, Nano Lett. (2016).
[15] R. Po, C. Carbonera, A. Bernardi, and N. Camaioni, Energy Environ. Sci. **4**, 285 (2011).
[16] P. Qin, G. Fang, Q. He, N. Sun, X. Fan, Q. Zheng, F. Chen, J. Wan, and X. Zhao, Sol. Energy Mater. Sol. Cells **95**, 1005 (2011).
[17] P. Qin, G. Fang, N. Sun, X. Fan, Q. Zheng, F. Chen, J. Wan, and X. Zhao, Thin Solid Films **519**, 4334 (2011).
[18] L. Chen, J. Yang, S. Klaus, L. J. Lee, R. Woods-Robinson, J. Ma, Y. Lum, J. K. Cooper, F. M. Toma, L.-W. Wang *et al.*, J. Am. Chem. Soc. **137**, 9595 (2015).
[19] R. G. Gordon, MRS Bull. **25**, 52 (2000).
[20] R. Nagarajan, N. Duan, M. Jayaraj, J. Li, K. Vanaja, A. Yokochi, A. Draeseke, J. Tate, and A. Sleight, Int. J. Inorgan. Mater. **3**, 265 (2001).
[21] L. Farrell, K. Fleischer, D. Caffrey, D. Mullarkey, E. Norton, and I. V. Shvets, Phys. Rev. B **91**, 125202 (2015).
[22] L. Farrell, E. Norton, B. J. O'Dowd, D. Caffrey, I. V. Shvets, and K. Fleischer, Appl. Phys. Lett. **107**, 031901 (2015).
[23] S. Lim, S. Desu, and A. Rastogi, J. Phys. Chem. Solids **69**, 2047 (2008).
[24] D. O. Scanlon, A. Walsh, B. J. Morgan, G. W. Watson, D. J. Payne, and R. G. Egdell, Phys. Rev. B **79**, 035101 (2009).
[25] H. Hiraga, T. Makino, T. Fukumura, H. Weng, and M. Kawasaki, Phys. Rev. B **84**, 041411 (2011).
[26] T. Arnold, D. J. Payne, A. Bourlange, J. P. Hu, R. G. Egdell, L. F. J. Piper, L. Colakerol, A. De Masi, P.-A. Glans, T. Learmonth *et al.*, Phys. Rev. B **79**, 075102 (2009).
[27] D. O. Scanlon and G. W. Watson, J. Mater. Chem. **21**, 3655 (2011).
[28] T. Yokobori, M. Okawa, K. Konishi, R. Takei, K. Katayama, S. Oozono, T. Shinmura, T. Okuda, H. Wadati, E. Sakai *et al.*, Phys. Rev. B **87**, 195124 (2013).
[29] E. Arca, K. Fleischer, and I. V. Shvets, Appl. Phys. Lett. **99**, 111910 (2011).
[30] N. Uekawa and K. Kaneko, J. Phys. Chem. **100**, 4193 (1996).
[31] K. H. L. Zhang, Y. Du, A. Papadogianni, O. Bierwagen, S. Sallis, L. F. J. Piper, M. E. Bowden, V. Shutthanandan, P. V. Sushko, and S. A. Chambers, Adv. Mater. **27**, 5191 (2015).
[32] H. Peng, A. Zakutayev, S. Lany, T. R. Paudel, M. d'Avezac, P. F. Ndione, J. D. Perkins, D. S. Ginley, A. R. Nagaraja, N. H. Perry *et al.*, Adv. Func. Mater. **23**, 5267 (2013).
[33] A. R. Nagaraja, K. H. Stone, M. F. Toney, H. Peng, S. Lany, and T. O. Mason, Chem. Mater. **26**, 4598 (2014).
[34] L. Farrell, E. Norton, C. M. Smith, D. Caffrey, I. V. Shvets, and K. Fleischer, J. Mater. Chem. C **4**, 126 (2016).
[35] K. Fleischer, D. Caffrey, L. Farrell, E. Norton, D. Mullarkey, E. Arca, and I. V. Shvets, Thin Solid Films **594**, 245 (2015).
[36] E. Stavitski and F. M. de Groot, Micron **41**, 687 (2010).
[37] M. Grioni, J. F. van Acker, M. T. Czyzyk, and J. C. Fuggle, Phys. Rev. B **45**, 3309 (1992).
[38] S. L. Hulbert, B. A. Bunker, F. C. Brown, and P. Pianetta, Phys. Rev. B **30**, 2120 (1984).
[39] J. P. Hu, D. J. Payne, R. G. Egdell, P.-A. Glans, T. Learmonth, K. E. Smith, J. Guo, and N. M. Harrison, Phys. Rev. B **77**, 155115 (2008).
[40] M. Nolan and S. D. Elliott, Chem. Mater. **20**, 5522 (2008).
[41] M. Brik, N. Avram, and C. Avram, Solid State Commun. **132**, 831 (2004).
[42] P. S. Bagus, E. S. Ilton, and J. R. Rustad, Phys. Rev. B **69**, 205112 (2004).
[43] H. Ikeno, T. Mizoguchi, and I. Tanaka, Phys. Rev. B **83**, 155107 (2011).
[44] M. Matsubara, T. Uozumi, A. Kotani, and J. Claude Parlebas, J. Phys. Soc. Jpn. **74**, 2052 (2005).
[45] J. Campbell and T. Papp, At. Data Nucl. Data Tables **77**, 1 (2001).
[46] X. Li, L. Liu, and V. E. Henrich, Solid State Commun. **84**, 1103 (1992).
[47] E. Bertel, R. Stockbauer, R. L. Kurtz, D. E. Ramaker, and T. E. Madey, Phys. Rev. B **31**, 5580 (1985).
[48] S. Chambers, J. Williams, M. Henderson, A. Joly, M. Varela, and S. Pennycook, Surface Sci. **587**, L197 (2005).
[49] A. Barnabé, Y. Thimont, M. Lalanne, L. Presmanes, and P. Tailhades, J. Mater. Chem. C **3**, 6012 (2015).